









Investigation and field effect tuning of thermoelectric properties of SnSe₂ flakes

Ilaria Pallecchi , Federico Caglieris , Michele Ceccardi , Nicola Manca, Daniele Marré , Luca Repetto ,
and Marine Schott 

CNR-SPIN and University of Genoa, Via Dodecaneso 33, 16146, Genoa, Italy

Daniel I. Bilc 

Faculty of Physics, Babeş-Bolyai University, 1 Kogălniceanu, RO-400084 Cluj-Napoca, Romania Independent Contribution, RO-407280 Floreşti, Romania

Stefanos Chaitoglou  and Athanasios Dimoulas 

Institute of Nanoscience and Nanotechnology, National Center for Scientific Research 'DEMOKRITOS', 15310, Athens, Greece

Matthieu J. Verstraete 

Nanomat, Q-Mat, CESAM, and European Theoretical Spectroscopy Facility, Université de Liège (B5), B-4000 Liège, Belgium



(Received 3 January 2023; accepted 26 April 2023; published 15 May 2023)

The family of van der Waals dichalcogenides (vdWDs) includes a large number of compositions and phases, exhibiting varied properties and functionalities. They have opened up a novel electronics of two-dimensional materials, characterized by higher integration and interfaces which are atomically sharper and cleaner than conventional electronics. Among these functionalities, some vdWDs possess remarkable thermoelectric properties. SnSe₂ has been identified as a promising thermoelectric material on the basis of its estimated electronic and transport properties. In this work we carry out experimental measurements of the electric and thermoelectric properties of SnSe₂ flakes. For a 30- μm -thick SnSe₂ flake at room temperature, we measure electron mobility of 40 cm² V⁻¹ s⁻¹, a carrier density of 4×10^{18} cm⁻³, a Seebeck coefficient $S \approx -400$ $\mu\text{V/K}$, and thermoelectric power factor $S^2\sigma \approx 0.35$ mW m⁻¹ K⁻². The comparison of experimental results with theoretical calculations shows fair agreement and indicates that the dominant carrier scattering mechanisms are polar optical phonons at room temperature and ionized impurities below 50 K. In order to explore possible improvement of the thermoelectric properties, we carry out reversible electrostatic doping on a thinner flake, in a field effect setup. On this 75-nm-thick SnSe₂ flake, we measure a field effect variation of the Seebeck coefficient of up to 290% at low temperature, and a corresponding variation of the thermoelectric power factor of up to 1050%. We find that the power factor increases with the depletion of n -type charge carriers. Field effect control of thermoelectric transport opens perspectives for boosting energy harvesting and novel switching technologies based on two-dimensional materials.

DOI: [10.1103/PhysRevMaterials.7.054004](https://doi.org/10.1103/PhysRevMaterials.7.054004)

I. INTRODUCTION

Graphene and related two-dimensional compounds represent a unique material platform for multifold technological applications, ranging from electronics, optoelectronics, or spintronics to energy generation, energy storage, and sensors. As a further functionality that has not yet been widely explored, van der Waals dichalcogenides (vdWDs) present features which should make them good thermoelectrics [1]. Indeed, vdWDs have an electronic band gap in the visible spectrum, with both n -type and p -type transport, quite large effective masses, and band degeneracy. Additionally, they have moderate thermal conductivity (few tens of W m⁻¹ K⁻¹), which can be further reduced by microstructuring or epitaxy engineering [2–4]. Their electronic band structures and phonon spectra are sensitive to confinement [5,6], so that their thermoelectric properties can be tuned by varying sample thickness in the range of a few atomic layers. The thermal conductivity κ was found to decrease with thickness in SnSe₂

[7], but, on the other hand, it was demonstrated that thickness must not necessarily be in the few atomic layers range to have the lowest κ . In MoSe₂ κ exhibits a saturating behavior with decreasing thickness below 30 atomic layers [8]. Extremely large tunability of transport properties is also obtained by field effect in flakes just a few atomic layers thick, which allows to identify optimal values of the chemical potential to boost thermoelectric performance. These field effect experiments show that values of thermoelectric power factors of vdWDs at room temperature can be comparable to those of commercial thermoelectrics [9–11].

In previous work, we carried out theoretical studies to identify those vdWDs that possess the highest thermoelectric performances. WSe₂, MoTe₂, and SnSe₂ were predicted to exhibit remarkable values of thermoelectric power factor and figure of merit, further tunable by thickness and lattice strain [12]. Among these vdWDs, the thermoelectric properties of SnSe₂ appear to be particularly promising, and this compound is chemically akin to its layered monochalco-

genide counterpart SnSe. The latter's thermoelectric figure of merit reaches 2.6 at 923 K in *p*-type single crystals, and was a breakthrough in the search for new thermoelectric materials [13,14]. Remarkably in view of applications, both *p*-type and *n*-type SnSe polycrystals can be optimized for high-temperature operation by chemical doping [15,16]. Nanostructuring was also attempted to improve thermoelectric performance of SnSe films [17] and nanoflakes [18,19]. In its dichalcogenide sibling SnSe₂, thermoelectric properties of samples in single-crystalline form were experimentally explored only by Pham *et al.* [20]. The high-quality SnSe₂ flakes in their work exhibited thermoelectric power factors (product of squared Seebeck coefficient S^2 and electrical conductivity σ) $S^2\sigma \sim 0.15 \text{ mW m}^{-1} \text{ K}^{-2}$ at room temperature and $0.34 \text{ mW m}^{-1} \text{ K}^{-2}$ at 673 K in the in-plane direction, while the corresponding figures of merit $ZT = S^2\sigma T/\kappa$ (κ thermal conductivity, T absolute temperature) were $ZT \sim 0.01$ and 0.1 at room temperature and 673 K, respectively. Their analysis of angle-resolved photoemission spectroscopy indicated that the thermoelectric performance might be further improved by electron doping. The effect of chemical doping was exclusively explored in samples fabricated in the form of highly oriented nanosheet pellets by spark plasma sintering [21–23]. Undoped, chlorine-doped, barium-doped, and Cu-intercalated SnSe₂ pellets all resulted to be *n* type. Enhanced power factors along the in-plane direction were achieved by simultaneously introducing Se deficiency and chlorine doping, while reduced thermal conductivity was obtained thanks to efficient phonon scattering at grain boundaries. At room temperature, $S^2\sigma \approx 0.8 \text{ mW m}^{-1} \text{ K}^{-2}$ and $\kappa \approx 2 \text{ W m}^{-1} \text{ K}^{-1}$ resulted in $ZT \approx 0.15$, and at 673 K a remarkable $ZT \approx 0.63$ was obtained [22]. Simultaneous copper intercalation and barium substitution led to a power factor $\approx 1.2 \text{ mW m}^{-1} \text{ K}^{-2}$, almost temperature independent from 300 to 773 K, which was the highest reported for all polycrystalline SnSe₂- and SnSe-based materials, with corresponding figures of merit $ZT \approx 0.10$ at 300 K and $ZT \approx 0.67$ at 773 K [23]. The effect of the microstructure on thermoelectric properties was also investigated by Chen *et al.* in SnSe₂ films deposited by physical vapor deposition and annealing in Se partial pressure [24]. In these films, structural disorder was introduced by random in-plane orientation among successive layers, while maintaining a high degree of *c*-axis orientation. After Se annealing, which mitigated Se vacancies and promoted the SnSe-to-SnSe₂ phase transition, cross-plane Seebeck coefficients up to $-630 \mu\text{V/K}$ and power factors up to $2 \times 10^{-4} \text{ mW m}^{-1} \text{ K}^{-2}$ at room temperature were measured.

From the above summary of available literature on theoretical and experimental studies on SnSe₂, it emerges that this compound has strong potential as a thermoelectric material, but the effect of doping on single-crystalline SnSe₂ flakes has not been investigated. Since SnSe₂ and other high-potential dichalcogenides (WSe₂, MoTe₂) have low dielectric permittivities, their polycrystalline forms will have significant grain-boundary electrical resistance due to imperfect screening at interfaces, which will decrease their thermoelectric performance. For such materials, nanostructuring achieved by grain-size minimization is not necessarily the best route to improve thermoelectric performance. For this reason, the optimization of single-crystalline SnSe₂ flakes is very im-

portant [12,25]. Furthermore, a field effect setup offers the opportunity to carry out clean and reversible doping to tune electric and thermoelectric properties of SnSe₂ flakes by band filling. In order to implement this strategy and confirm theoretical predictions [12], in this work we carry out experimental measurements of the electric and thermoelectric properties of micrometric-thick SnSe₂ flakes and explore possible improvement of these properties in thinner SnSe₂ flakes under field effect. We compare the experimental results with theoretical calculations including quantitative doping and scattering rates for SnSe₂.

II. EXPERIMENTAL METHODS

Crystals of 1T -SnSe₂ were purchased from HQ Graphene, and flakes of different thickness and lateral size were mechanically exfoliated and transferred for characterization onto SrTiO₃ substrates (see below). Larger flakes of micrometric thickness and hundreds of micrometers lateral size were mechanically exfoliated and transferred on quartz substrates. Additional capping layers of hexagonal boron nitride (h-BN) were transferred on top of these large flakes, as protection against charged surface impurities. For smaller flakes of few tens of nanometer thickness and few tens of micrometer lateral size, SrTiO₃ was chosen as a substrate suitable for field effect experiments, due to its high relative dielectric permittivity $\epsilon_r \sim 300$ at room temperature and up to $\epsilon_r \sim 20\,000$ at low temperature and low electric field [26]. Patterns of micrometric electrical contacts were realized by optical lithography, thermal evaporation of CrO/Au, and lift-off. CrO/Au serpentine heaters were also fabricated and calibrated to be used as heaters and thermometers for thermoelectric measurements in flakes of micrometric size. The exfoliated flakes were transferred onto the micrometric patterns using a micromanipulator. Successively, finer electrical contacting was realized by focused ion-beam deposition of metallic tungsten. Flake thicknesses were measured from atomic force microscope profiles.

Resistance, Hall effect, magnetoresistance, and thermopower measurements from room temperature down to 10 K and in magnetic fields up to 9 T were carried out in a commercial physical property measurement system (PPMS) by Quantum Design, with home-made adaptations to the sample holder and acquisition software. A four-probe geometry was used for electrical contacts. Thermopower measurements were performed in high vacuum and a steady-state technique was used to feed heat into the free-standing sample and establish a temperature gradient. A CrO/Au serpentine heater was placed on one sample edge, while the opposite edge was linked to the thermal sink through a clamp. A sinusoidal current with 100-s period was applied to the heater, and the response extracted by fast Fourier transform of the voltage signals measured at the leads and of the temperature signals. The latter were measured using the calibrated CrO/Au thermometers for flakes of tens of micrometer size, or with thermocouples for flakes of hundreds of micrometer size, respectively.

Electric and thermoelectric transport measurements were also carried out under field effect, by applying a voltage to a metallic gate electrode placed on the back of the 0.5-mm-thick SrTiO₃ substrate. A positive (negative) gate electric field

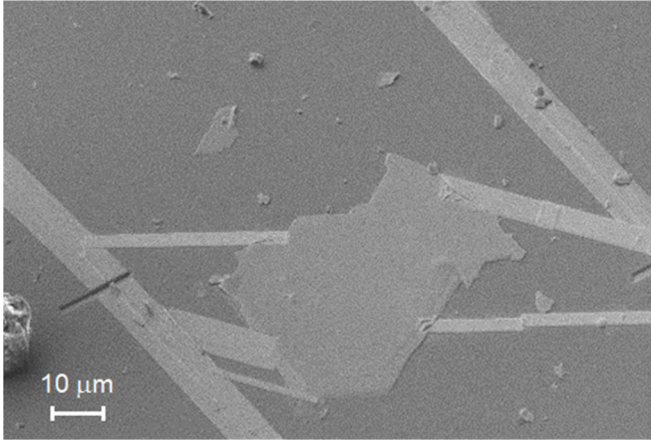


FIG. 1. Scanning electron microscopy (SEM) image of the exfoliated SnSe₂ flake of micrometric size within a pattern of contacts realized by optical lithography and FIB.

accumulates (depletes) n -type mobile charge carriers in the vdWD at the vdWD/SrTiO₃ interface, thus tuning the electric and thermoelectric properties, which depend on the carrier concentration. As the electric field decays into the vdWD, due to screening by mobile charge carriers, the relative tuning of the electric and thermoelectric properties depends on how deep the electric field penetrates into the vdWD as compared to the total thickness of the vdWD flake itself; hence, a larger relative tuning is obtained for flakes of smaller thickness and smaller carrier density.

Figure 1 shows a contacted micrometric flake. Due to the irregular sample shape, we estimate a 30% uncertainty on the magnitude of electrical transport properties, related to geometrical factors. Furthermore, from the measurement of a sizable number of SnSe₂ samples, we observe also some sample-to-sample variations in the exact temperature dependence of electric and thermoelectric transport properties, which could be due to accidental factors at the micrometric or nanometric scale, such as bending of the flake or inhomogeneity in the impurity distribution.

III. THEORETICAL METHODS

The electronic and thermoelectric properties of SnSe₂ bulk were studied within density-functional theory (DFT) formalism using the B1-WC hybrid functional [27]. B1-WC describes the electronic (band gaps) and structural properties with better accuracy than the usual semilocal exchange-correlation functionals, and it is more appropriate for correlated materials with d electronic states [28,29]. The electronic structure calculations were performed using the linear combination of atomic orbitals method as implemented in the CRYSTAL code [30]. We use localized Gaussian-type basis sets including polarization orbitals and considered all the electrons for Se [31], and a Hartree-Fock pseudopotential for Sn [32]. The exponents of the most diffuse valence and polarization Gaussian functions were optimized within B1-WC to minimize the total energy of SnSe₂ bulk. The optimized exponents are, respectively, 1.5963, 0.7686, 0.3199, 0.1, 1.5136, 1.0497, and 0.2607 for $4s$, $4p$, $5sp$, $6sp$, $4d$, $5d$,

and $6d$ functions of Se; 2.5335, 0.2056, 0.8050, and 0.2259 for $5p$, $6sp$, $5d$, and $6d$ functions of Sn. To increase the efficiency of the CRYSTAL code, the two outermost s - and p functions were combined into $5sp$ (for Se) and $6sp$ functions (for Sn).

Brillouin-zone integration was performed using a $6 \times 6 \times 6$ mesh of k points. The self-consistent-field calculations were considered to be converged when the energy changes between interactions were smaller than 10^{-8} hartree. An extra-large predefined and pruned grid consisting of 75 radial points and 974 angular points was used for the numerical integration of the charge density. Full optimizations of the lattice constants and atomic positions were performed with the convergence criteria of 5×10^{-5} hartree/bohr in the root-mean-square values of forces and 1.2×10^{-3} bohr in the root-mean square values of atomic displacements. The level of accuracy in evaluating the Coulomb and exchange series is controlled by five tolerance parameters (10^{-ITOL_j} , $j = 1 - 5$). The values of the parameters ITOL used in our calculations were 7, 7, 7, 9, and 30.

The transport properties were calculated within the Boltzmann transport formalism and the constant relaxation time approximation, using the BOLTZTRAP transport code [33]. We fixed the relaxation times on the basis of the experimental resistivity curves and included a generic $1/T$ temperature dependence for the acoustic and optical phonon scatterings at high T . We use $\tau_{ac} = \tau_{ac}^{\text{ref}} (T/T_{\text{ref}})^{-1} E_r^{-1/2}$ for the degenerate case, and $\tau_{ac} = \tau_{ac}^{\text{ref}} (T/T_{\text{ref}})^{-3/2} E_r^{-1/2}$ for the nondegenerate case; then, $\tau_{po} = \tau_{po}^{\text{ref}} (T/T_{\text{ref}})^{-1/2} E_r^{1/2}$ for the polar optical phonon scattering. Ionized impurity relaxation times are given by $\tau_{\text{imp}} = \tau_{\text{imp}}^{\text{ref}} (T/T_{\text{ref}})^{3/2} E_r^{3/2}$. In all of the above, T_{ref} is a reference temperature at which the scattering times are known (calculated or fit to experiment), and E_r is the reduced energy, $E_r = E/k_B T$ [34–36]. The transport coefficients were very well converged using energies calculated on a mesh of $47 \times 47 \times 41$ k points.

IV. RESULTS AND DISCUSSION

A. Bulk SnSe₂ flake

We first present the electric and thermoelectric characterization of a large SnSe₂ flake of 30- μm thickness and hundreds of micrometers lateral size, representative of bulk-like behavior, capped with h-BN to preserve high mobility. Figure 2 (main panel) shows resistivity measurements of the SnSe₂/BN flake, exhibiting a semiconducting temperature dependence below around 130 K. The resistivity curve cannot be described by a thermally activated transport behavior with a single energy-gap value across the whole temperature range 10–310 K. However, in smaller temperature subranges the data can be reproduced with thermally activated transport with activation gaps from a few to a few tens of meV. These are much smaller than the intrinsic optical gap, and probably related to shallow impurity levels close to the band edges. The inverse Hall resistance $1/eR_H$ is shown in Fig. 2 (upper inset). The Hall effect is negative, indicating dominant n -type transport, and it is weakly temperature dependent. The room-temperature charge-carrier density, extracted in a single-band model, is around $4 \times 10^{18} \text{ cm}^{-3}$. Hall mobility, extracted in a

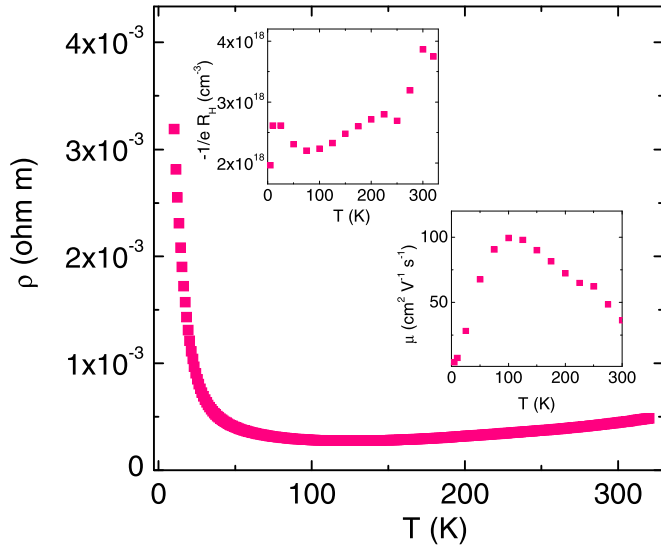


FIG. 2. Resistivity vs temperature curves measured in the 30- μm -thick $\text{SnSe}_2/\text{h-BN}$ flake. Upper inset: Carrier density of the same flakes, extracted from Hall resistance R_H . Lower inset: Hall mobility of the same flake.

single-band description and shown in Fig. 2 (lower inset), is around $40 \text{ cm}^2 \text{ V}^{-1} \text{ s}^{-1}$ at room temperature.

Figure 3 (left panel) shows the Seebeck effect measurement of the SnSe_2/BN flake. The Seebeck coefficient S is negative and large, comparable to robust thermoelectric materials. At room temperature, the magnitude of S is $\approx -400 \mu\text{V}/\text{K}$. The thermoelectric power factor $S^2\sigma$ is displayed in Fig. 3 (left panel). The room-temperature power factor $S^2\sigma \sim 0.35 \text{ mW m}^{-1} \text{ K}^{-2}$, combined with a low and anisotropic thermal conductivity [7], confirm this compound is promising for thermoelectric applications. This power factor is comparable with literature values on bulklike samples, for example $S^2\sigma \sim 0.15 \text{ mW m}^{-1} \text{ K}^{-2}$ for a high-quality SnSe_2 flake [20] and $S^2\sigma \sim 0.8 \text{ mW m}^{-1} \text{ K}^{-2}$ for highly oriented and dense SnSe_2 pellets [22]. However, high thermoelectric performances among vdWDs are displayed by few-layers-thick MoS_2 and WSe_2 flakes, where S values around $500 \mu\text{V}/\text{K}$ and $S^2\sigma$ values as large as several $\text{mW m}^{-1} \text{ K}^{-2}$ are observed under field effect [9–11].

In order to get insight into transport mechanisms, we compare the calculated electrical resistivity ρ , thermopower S , power factor $S^2\sigma$, and electron mobility μ values of SnSe_2 bulk with experimental results (Figs. 2 and 3). This comparison requires fixing the chemical potential to match the electron carrier density n of the measured sample at 300 K. This yields fair agreement with the measured electric and thermoelectric transport properties, as shown in Fig. 4. At higher temperature, reproducing the increasingly metallic resistivity behavior would require other models. The electrical resistivity was estimated considering the temperature T and energy E dependences of polar optical and ionized impurity relaxation times (see Sec. III). We find that the T dependence of resistivity in the [120 K, 300 K] temperature interval is dominated by polar optical scattering: by fitting the experimental electrical resistivity value at 300 K, we estimate a reference polar optical relaxation time $\tau_{po}^{\text{ref}} \sim 0.38 \times 10^{-14} \text{ s}$. At low T

ionized impurity scattering dominates: by fitting the experimental electrical resistivity at 20 K we estimated a reference impurity relaxation time $\tau_{\text{imp}}^{\text{ref}} \sim 8.7 \times 10^{-14} \text{ s}$. For comparison, the resistivity with acoustic phonon scattering is shown in the same figure, but it gives a decrease of resistivity with T in the [120 K, 300 K] temperature interval, and is discarded from further fits. Usually, the deformation potentials of acoustic and optical phonon scatterings are dominant at much higher temperature (e.g., for $T > 600 \text{ K}$). The total relaxation time τ is given through Matthiessen's rule: $1/\tau = 1/\tau_{po} + 1/\tau_{\text{imp}}$. We used the total (energy-dependent) relaxation time in the estimation of the resistivity, thermopower, power factor, and carrier mobility of bulk SnSe_2 [Figs. 4(a)–4(d)]. The latter two are more sensitive to the fit as they involve ratios of n , S , and ρ . Things could be further improved if the temperature dependence of the carrier density $n(T)$ was included, to yield a temperature-dependent $\tau_{po}^{\text{ref}}(T)$.

B. Tuning of SnSe_2 transport properties by field effect

In order to investigate whether the measured electric and thermoelectric properties can be improved by doping, we carried out reversible electrostatic doping in field effect experiments. To maximize the field effect tuning of the properties, we selected a thinner flake transferred on a substrate with high dielectric permittivity. Figure 5 (left panel) shows resistivity measurements of a 75-nm SnSe_2 flake, exhibiting semiconducting behavior. As for the thicker flake presented in the previous section, it appears that a single transport mechanism cannot describe the whole temperature dependence of resistivity from 10 to 300 K. The curve can be described by a small polaron hopping (SPH) mechanism $\rho(T) \propto T \exp(\frac{E_{\text{SPH}}}{k_B T})$ [37] with energy gaps $E_{\text{SPH}} \approx 2$ and 10 meV dominating at low temperatures ($T < 120 \text{ K}$) and a thermal activation mechanism $\rho(T) \propto \exp(\frac{E_{\text{gap}}}{k_B T})$ with energy gap $E_{\text{gap}} \approx 30 \text{ meV}$ dominating at high temperatures ($T > 120 \text{ K}$). From Hall-effect measurements, we find an n -type carrier density ranging from around $2 \times 10^{17} \text{ cm}^{-3}$ at low temperature to $7 \times 10^{18} \text{ cm}^{-3}$ at high temperature, presented in Fig. 5 (right panel). Mobility, shown in the inset, is on the order of $1 \text{ cm}^2 \text{ V}^{-1} \text{ s}^{-1}$. In general, from the comparison of transport properties of the thicker (Fig. 2) and thinner (Fig. 5) flakes, as well as from the characterization of other 15 SnSe_2 flakes, it can be said that the effect varying the thickness from several tens of micrometers to several tens of nanometers is a stronger sensitivity of the transport properties to surface and interface impurities or oxidized superficial layers, so that samples in the tens of nanometers thickness range exhibit higher resistivity and lower mobility.

The variation of resistance by reversible accumulation and depletion of charge carriers by field effect was measured at different temperatures from 10 to 200 K. At temperatures higher than 200 K, the experiment could not be performed due to leakage current across the substrate, which is common for SrTiO_3 close to room temperature. Resistance versus gate-voltage data are displayed in Fig. 6 for the same 75-nm-thick SnSe_2 flake. With a back-gate voltage in the range $\pm 200 \text{ V}$, the relative variation of resistance $\Delta R/R = ((R(V_{\text{gate}} = -200 \text{ V}) - R(V_{\text{gate}} = +200 \text{ V}))/R(V_{\text{gate}} = 0))$ is 5.2% at

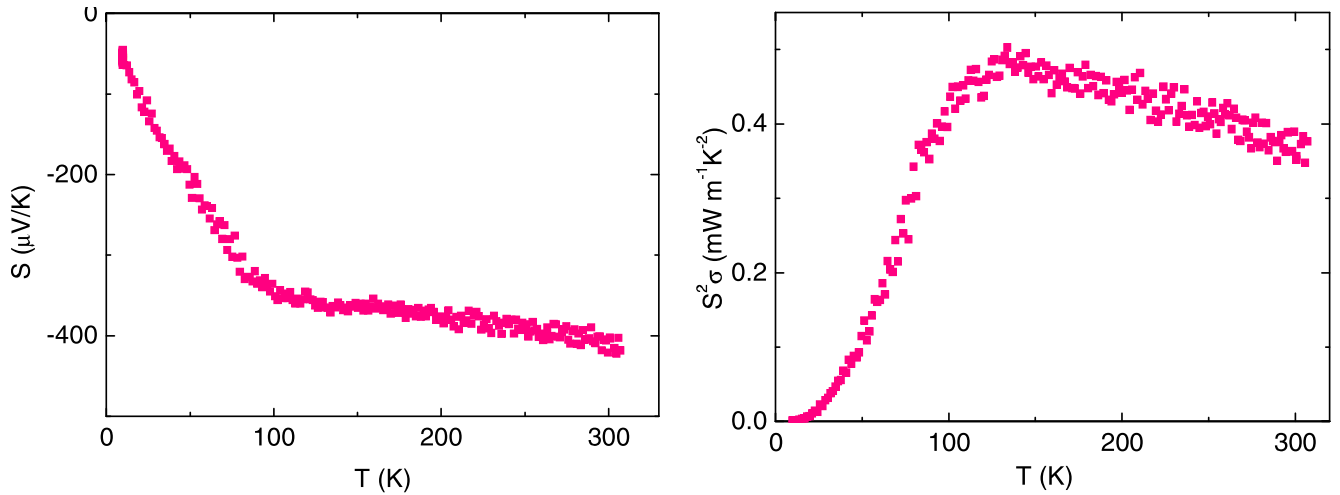


FIG. 3. Left: Seebeck coefficient S vs temperatures curves measured in the in the 30- μ m-thick SnSe₂/h-BN flake. Right: Power factor $S^2\sigma$ of the same flake.

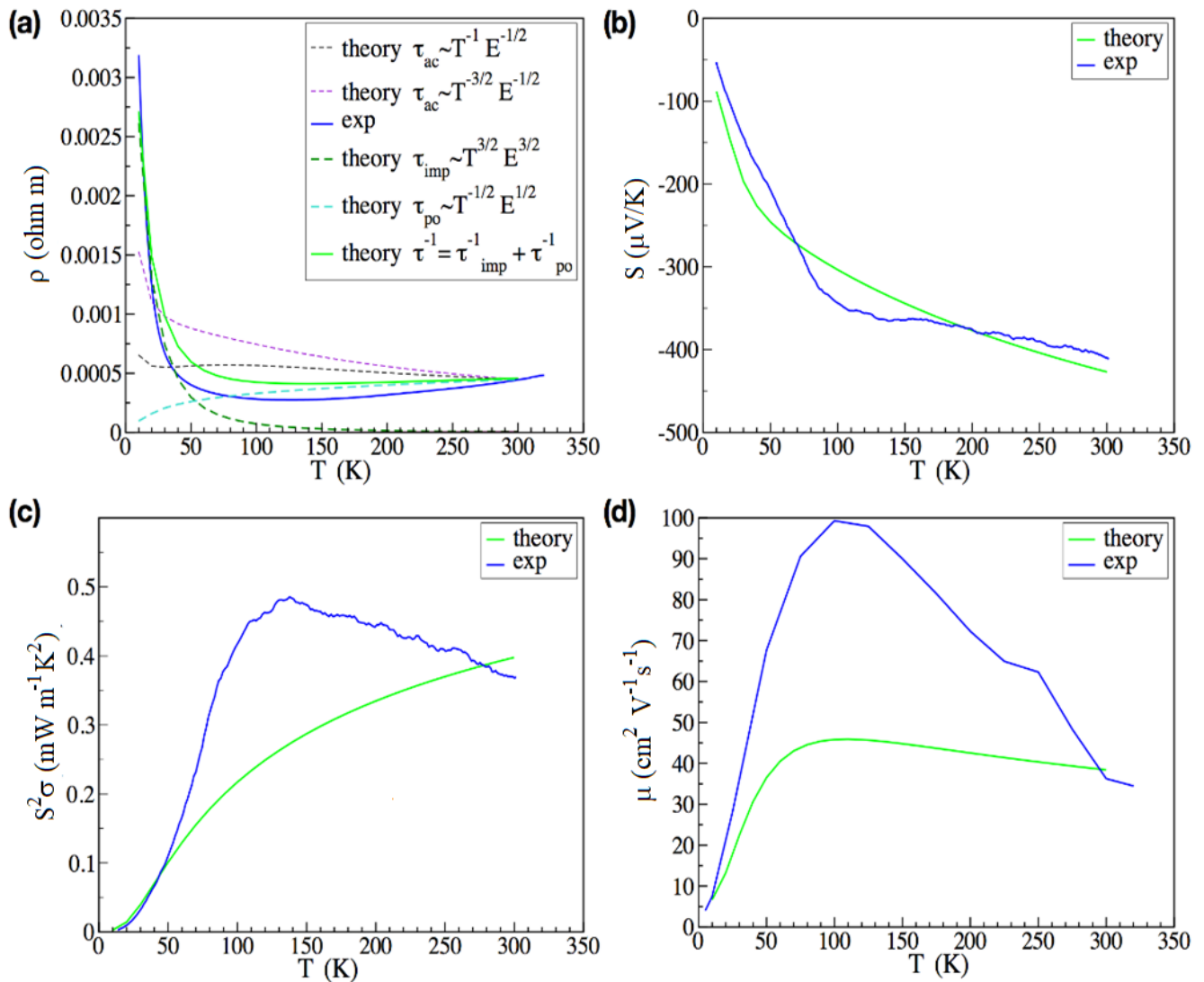


FIG. 4. Temperature dependence of thermoelectric properties of SnSe₂: (a) resistivity, (b) thermopower S , (c) power factor $S^2\sigma$, and (d) carrier mobility. Theoretical values are estimated for SnSe₂ bulk at an electron carrier density $n = 3.86 \times 10^{18} \text{ cm}^{-3}$, which matches the experimental carrier density at 300 K. Experimental data correspond to the SnSe₂ flake from Figs. 2 and 3.

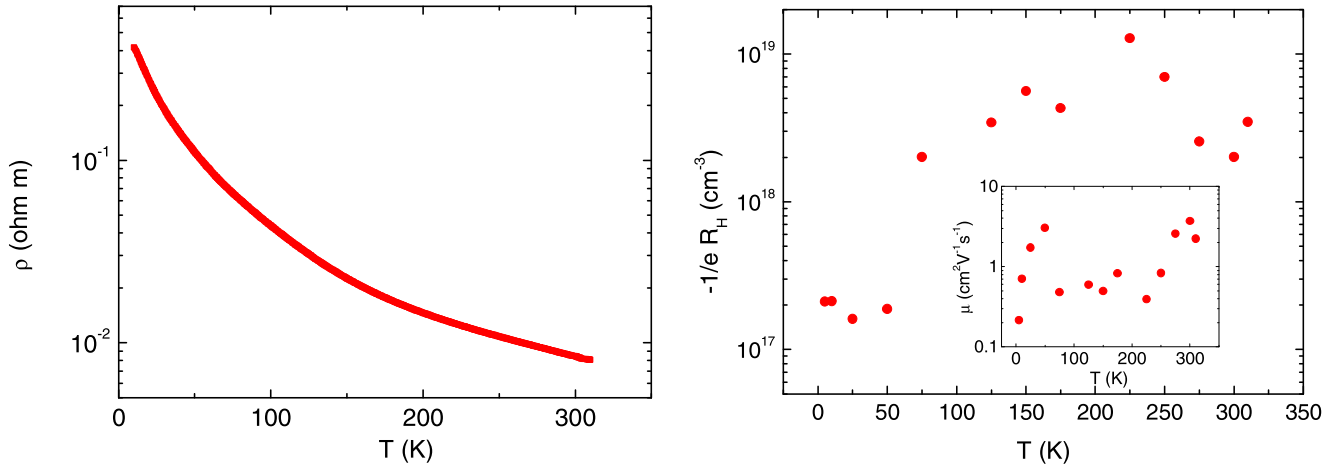


FIG. 5. Left: resistivity vs temperature of a 75-nm-thick SnSe₂ flake. Right: Carrier density (main panel) and mobility (inset) of the same flake, extracted from Hall resistance R_H .

10 K, 2.5% at 50 K, 1.8% at 100 K, and 0.64% at 200 K (see Fig. 6). Hysteresis was observed in different forward and backward sweeps of gate voltage due to trapping-detrapping of charges at the SrTiO₃/SnSe₂ interface and possibly also electromigration of charged traps. At all temperatures the measured relative variation of resistance is much smaller than the relative variation of carrier density expected on the basis of a parallel capacitor model, taking into account the carrier concentration measured by Hall effect and the temperature dependence of the SrTiO₃ dielectric constant [26]. This discrepancy between expected and measured relative variations is likely due to imperfect adherence of the flake to the substrate during the exfoliation and transfer technique (which can probably be optimized). This leads

to the presence of a void dead layer at the SrTiO₃/SnSe₂ interface and of charged impurity traps at this interface which screen the gate electric field.

In the left panel of Fig. 7, the temperature dependence of the Seebeck coefficient of the SnSe₂ flake is shown, exhibiting a maximum as a function of temperature, $|S| \approx 650 \mu\text{V/K}$ at 110 K, and a room-temperature value of $|S| \approx 10 \mu\text{V/K}$. In the right panel, the power factor peaks at $S^2\sigma \sim 0.014 \text{ mW m}^{-1} \text{ K}^{-2}$ around 125 K. In the thicker flake the carrier density is an order of magnitude smaller, and S almost saturates above 100 K (Fig. 3, left). Instead in the thinner flake, with higher carrier density, S decays to a much lower value in approaching room temperature. By fitting the low-temperature nearly linear portions of Seebeck data for the two samples

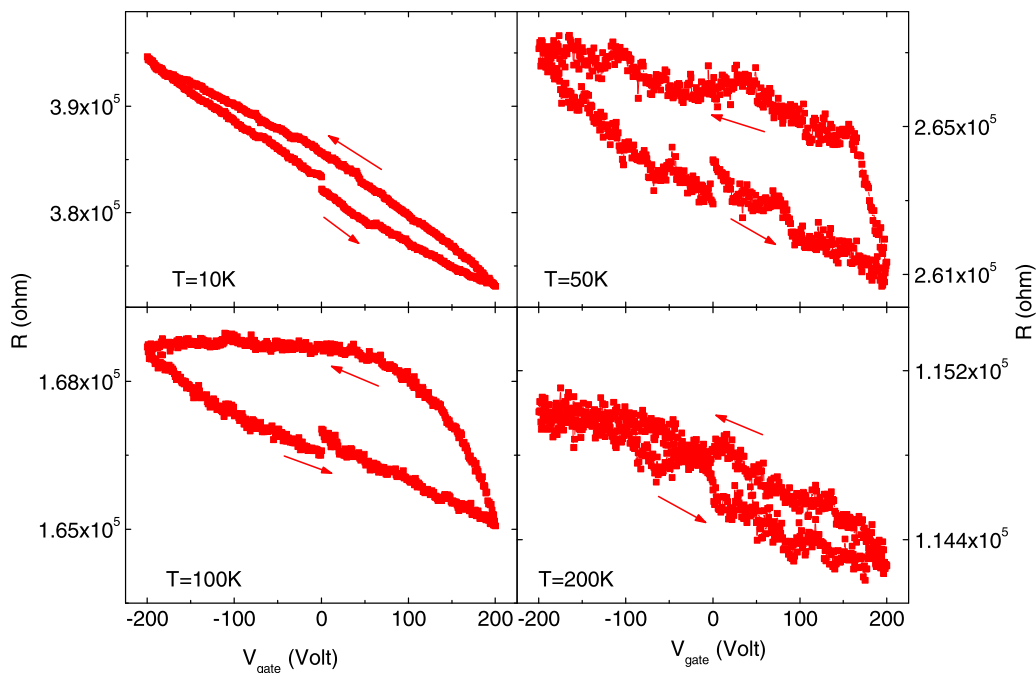


FIG. 6. Variation of resistance of the 75-nm-thick SnSe₂ flake with applied back-gate voltage at different temperatures. Arrows indicate the direction of the gate-voltage sweep.

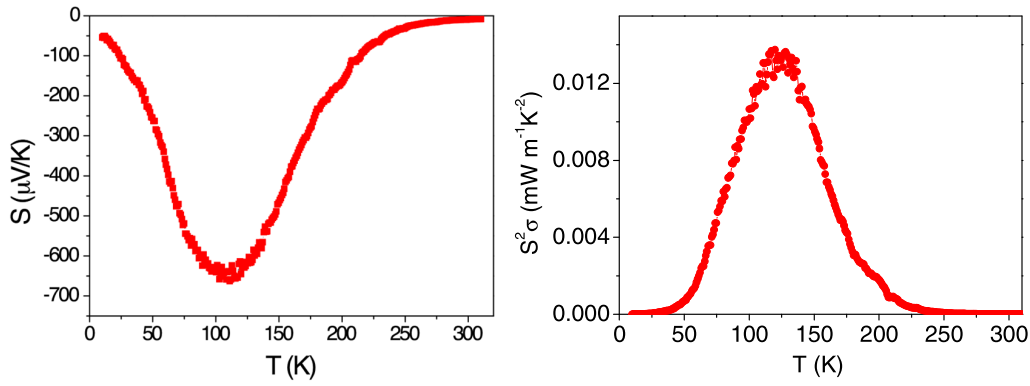


FIG. 7. Seebeck coefficient (left panel) and power factor (right panel) of the 75-nm-thick SnSe₂ flake as a function of temperature.

with the Cutler Mott relationship $S = -(\frac{3}{2} + \alpha) \frac{\pi^2 k_B^2 T}{3e} \frac{1}{E_F}$ (where k_B is the Boltzmann constant, e the electron charge, and α the exponent of the power-law energy dependence of the scattering time $\tau \propto E^\alpha$), we find Fermi energies $E_F \sim 20$ meV for the thin flake and $E_F \sim 29$ meV for the thick flake. For a spherical Fermi surface $E_F = \frac{\hbar^2}{2m_{\text{eff}}} (3\pi^2 n)^{2/3}$ (where m_{eff} is the effective mass at the Fermi level and \hbar is the Planck constant), hence the difference of the Fermi-level values does not fully account for the one order of magnitude difference in carrier concentrations at low temperatures. It is possible that different effective masses at the Fermi level, as well as different scattering mechanisms, as mentioned above, are dominant in the two samples. The thermoelectric power factor $S^2\sigma$ has a maximum at 110 K, with a value $1.1 \times 10^{-2} \text{ mW m}^{-1} \text{ K}^{-2}$, while it is $1.2 \times 10^{-5} \text{ mW m}^{-1} \text{ K}^{-2}$ at room temperature, and $6.0 \times 10^{-6} \text{ mW m}^{-1} \text{ K}^{-2}$ at 10 K. The Goldsmid-Sharp criterion [38] can be used to estimate the band gap E_g ($E_g = 2e|S_{\text{max}}|T_{\text{max}}$), resulting in a band gap of

~ 0.15 eV, which is much smaller than the intrinsic SnSe₂ band gap of ~ 1 eV (1.2 eV within B1-WC DFT [12]). This suggests the presence of in-gap states in the thinner SnSe₂ flake, which may lead to polaronic carriers similar to what was seen in SnSe₂ monolayers on Nb-doped SrTiO₃ substrates [39]. Such narrow-bandwidth polaronic states can explain the low mobilities of the thinner SnSe₂ flake (lower inset of Fig. 2). The nonmonotonic temperature dependence of S (Fig. 7) as well can be explained in terms of the small band gap: near ~ 110 K, S begins to decrease because of electronic thermal excitation across the small band gap of ~ 0.15 eV, and bipolar (electron and hole) contributions with opposite signs result in the decrease of S .

Figure 8 shows the variation of S with applied back-gate voltage in the range ± 200 V, at different temperatures. The total relative variation $|\Delta S/S| = (|S|(V_{\text{gate}} = -200 \text{ V}) - |S|(V_{\text{gate}} = +200 \text{ V})) / |S|(V_{\text{gate}} = 0)$ is 290% at 10 K, 240% at 50 K, 24% at 100 K, and 9% at 200 K (see Fig. 9), much larger than the relative variation of resistance. This discrep-

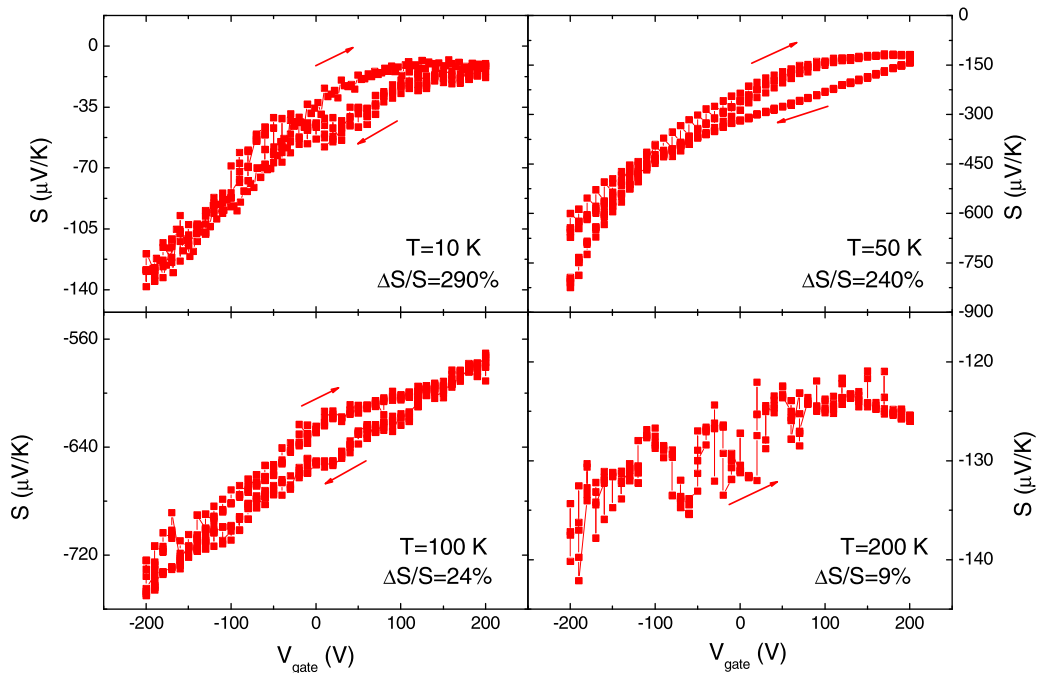


FIG. 8. Variation of Seebeck coefficient of the 75-nm-thick SnSe₂ flake with applied back-gate voltage at different temperatures.

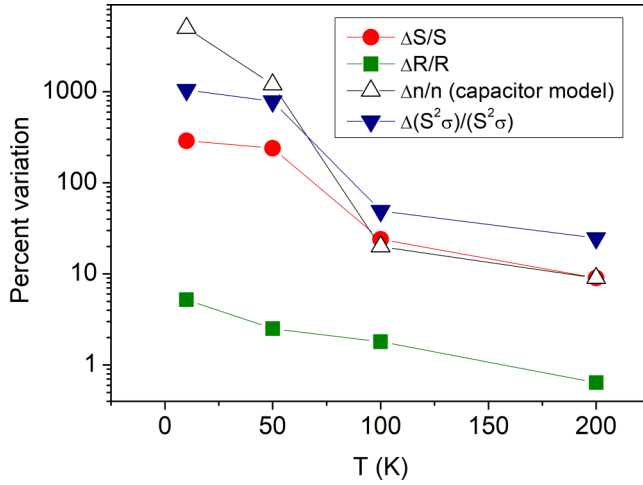


FIG. 9. Percent variation of Seebeck coefficient, resistance, and thermoelectric power factor under field effect up to ± 200 V, for the 75-nm-thick SnSe₂ flake, compared to the expected percent variation of the charge-carrier density, calculated on the basis of a parallel-plate capacitor model.

ancy is not implausible, considering that the variation of S is proportional to the variation of the *energy derivative* of the conductivity, instead of its absolute magnitude. Similar field effects were observed in other semiconducting vdWDs in literature [10,40,41], where variations in S were larger than in conductivity. It is worth noting that at the lower temperatures where the $|\Delta S/S|$ variation is largest the $|\Delta S/S|$ versus V_{gate} curves are asymmetric, with larger variations in the depletion regime (negative V_{gate}) than in the accumulation regime (positive V_{gate}). This could be a consequence of the Fermi level approaching the conduction band in the accumulation regime, thus sweeping an energy range of higher density of states.

We can estimate the variation of the power factor, to reveal the trend of thermoelectric properties with increasing or decreasing carrier concentration. We find that $S^2\sigma$ moves to higher values with decreasing electron doping, i.e., in the depletion regime, and to lower values in the accumulation regime, with a total variation by field effect that increases with decreasing temperature, also due to the higher dielectric constant of the SrTiO₃ substrate. The maximum variation of $S^2\sigma$ is a remarkable 1050% at 10 K. The reason for the increase of $S^2\sigma$ with decreasing electron density must be ascribed to the corresponding increase of Seebeck coefficient, and the relative change in $S^2\sigma$ is highest at low temperatures, where $S^2\sigma$ is smallest. The relative variations we obtain for the field effect on the Seebeck coefficient, resistance, and power factor are summarized in Fig. 9.

V. CONCLUSIONS

In this work, we present a combined experimental and theoretical approach to investigate the electric and thermoelectric properties of SnSe₂ flakes. We use the electric field effect in a

back-gate geometry to cleanly and reversibly tune the electric and thermoelectric properties by band filling and depletion.

SnSe₂ exfoliated flakes of micrometric and nanometric thickness exhibit n -type transport and semiconducting temperature dependence of the resistivity. In micrometric thick flakes capped with BN, at room temperature we measure mobility around $40 \text{ cm}^2 \text{ V}^{-1} \text{ s}^{-1}$, a carrier density around $4 \times 10^{18} \text{ cm}^{-3}$, a Seebeck coefficient $S \approx -400 \mu\text{V/K}$ and thermoelectric power factor $S^2\sigma \approx 0.35 \text{ mW m}^{-1} \text{ K}^{-2}$. Our theoretical calculations of the electric and thermoelectric transport properties are in fair agreement with the measured data. From the calculations, it turns out that the dominant carrier-scattering mechanisms are polar optical phonons in the 50–300 K temperature interval (τ_{po}^{ref} of $0.38 \times 10^{-14} \text{ s}$ at 300 K), and ionized impurities below 50 K ($\tau_{\text{imp}}^{\text{ref}} \sim 8.7 \times 10^{-14} \text{ s}$ at 20 K). For field effect experiments, a flake of nanometric thickness is chosen, exhibiting a Seebeck coefficient that peaks around 100 K with a value $|S| \approx 650 \mu\text{V/K}$ and a corresponding thermoelectric power factor $S^2\sigma \approx 0.011 \text{ mW m}^{-1} \text{ K}^{-2}$. These field effect experiments indicate that an improvement of thermoelectric properties can be achieved by doping. We find that the power factor increases with depletion of n -type charge carriers. We measure a field effect variation of the Seebeck coefficient up to 290% at low temperature, and a corresponding variation of the thermoelectric power factor up to 1050%. The ideal scenario would be to exploit an intermediate flake thickness (in the hundreds of nanometers), with the favorable starting point of bulk SnSe₂, but also a sensitivity to field effect tuning.

ACKNOWLEDGMENTS

This work was financially supported by the FLAG-ERA JTC2017 Project No. MELODICA “Revealing the potential of transition metal dichalcogenides for thermoelectric applications through nanostructuring and confinement.” [42] D.I.B. acknowledges financial support from a grant of the Romanian National Authority for Scientific Research and Innovation, CCCDI-UEFISCDI, Project No. COFUND-FLAGERA II-MELODICA, within PNCDI III. Computational resources were provided by the high-performance computational facility of Babes-Bolyai University (MADECIP, Grant No. POSCCE COD SMIS 48801/1862) cofinanced by the European Regional Development Fund. M.J.V. acknowledges funding from ULiege and the Federation Wallonie Bruxelles through ARC Grant No. DREAMS (G.A. 21/25-11), and a PRACE award granting access to MareNostrum4 at Barcelona Supercomputing Center (BSC), Spain (OptoSpin Project ID No. 2020225411). F.C. acknowledges the European Union’s Horizon 2020 research and innovation programme under the Marie Skłodowska-Curie Grant Agreement No. 892728. I.P. acknowledges the “Network 4 Energy Sustainable Transition-NEST” project, award number PE0000021, funded under the National Recovery and Resilience Plan (NRRP), Mission 4, Component 2, Investment 1.3 - Call for tender No. 1561 of 11.10.2022 of Italian Ministero dell’Università e della Ricerca (MUR); funded by the European Union-NextGenerationEU.

- [1] I. Pallecchi, N. Manca, B. Patil, L. Pellegrino, and D. Marré, Review on thermoelectric properties of transition metal dichalcogenides, *Nano Futures* **4**, 032008 (2020).
- [2] M. Sledzinska, R. Quey, B. Mortazavi, B. Graczykowski, M. Placidi, D. S. Reig, D. Navarro-Urrios, F. Alzina, L. Colombo, S. Roche, and C. M. Sotomayor Torres, Record low thermal conductivity of polycrystalline MoS₂ films: Tuning the thermal conductivity by grain orientation, *ACS Appl. Mater. Interfaces* **9**, 37905 (2017).
- [3] A. Aiyiti, S. Hu, C. Wang, Q. Xi, Z. Cheng, M. Xia, Y. Ma, J. Wu, J. Guo, Q. Wang, J. Zhou, J. Chen, X. Xu, and B. Li, Thermal conductivity of suspended few-layer MoS₂, *Nanoscale* **10**, 2727 (2018).
- [4] E. Hadland, H. Jang, M. Falmbigl, R. Fischer, D. L. Medlin, D. G. Cahill, and D. C. Johnson, Synthesis, characterization, and ultralow thermal conductivity of a lattice-mismatched SnSe₂(MoSe₂)_{1.32} heterostructure, *Chem. Mater.* **31**, 5699 (2019).
- [5] S. Manzeli, D. Ovchinnikov, D. Pasquier, O. V. Yazyev, and A. Kis, 2D transition metal dichalcogenides, *Nat. Rev. Mater.* **2**, 17033 (2017).
- [6] W. Huang, X. Luo, C. K. Gan, S. Y. Quek, and G. Liang, Theoretical study of thermoelectric properties of few-layer MoS₂ and WSe₂, *Phys. Chem. Chem. Phys.* **16**, 10866 (2014).
- [7] P. Xiao, E. Chavez-Angel, S. Chaitoglou, M. Sledzinska, A. Dimoulas, C. M. Sotomayor Torres, and A. El Sachat, Anisotropic thermal conductivity of crystalline layered SnSe₂, *Nano Lett.* **21**, 9172 (2021).
- [8] D. S. Reig, S. Varghese, R. Farris, A. Block, J. D. Mehew, O. Hellman, P. Woźniak, M. Sledzinska, A. El Sachat, E. Chávez-Ángel, S. O. Valenzuela, N. F. van Hulst, P. Ordejón, Z. Zanolli, C. M. Sotomayor Torres, M. J. Verstraete, and K.-J. Tielrooij, Unraveling heat transport and dissipation in suspended MoSe₂ from bulk to monolayer, *Adv. Mater.* **34**, 2108352 (2022).
- [9] K. Hippalgaonkar, Y. Wang, Y. Ye, D. Y. Qiu, H. Zhu, Y. Wang, J. Moore, S. G. Louie, and X. Zhang, High thermoelectric power factor in two-dimensional crystals of MoS₂, *Phys. Rev. B* **95**, 115407 (2017).
- [10] M. Kayyalha, J. Maassen, M. Lundstrom, L. Shi, and Y. P. Chen, Gate-tunable and thickness-dependent electronic and thermoelectric transport in few-layer MoS₂, *J. Appl. Phys.* **120**, 134305 (2016).
- [11] M. Yoshida, T. Iizuka, Y. Saito, M. Onga, R. Suzuki, Y. Zhang, Y. Iwasa, and S. Shimizu, Gate-optimized thermoelectric power factor in ultrathin WSe₂ single crystals, *Nano Lett.* **16**, 2061 (2016).
- [12] D. I. Bilc, D. Benea, V. Pop, P. Ghosez, and M. J. Verstraete, Electronic and thermoelectric properties of transition metal dichalcogenides, *J. Phys. Chem. C* **125**, 27084 (2021).
- [13] L.-D. Zhao, S.-H. Lo, Y. Zhang, H. Sun, G. Tan, C. Uher, C. Wolverton, V. P. Dravid, and M. G. Kanatzidis, Ultralow thermal conductivity and high thermoelectric figure of merit in SnSe crystals, *Nature (London)* **508**, 373 (2014).
- [14] L.-D. Zhao, G. Tan, S. Hao, J. He, Y. Pei, H. Chi, H. Wang, S. Gong, H. Xu, V. P. Dravid, C. Uher, G. J. Snyder, C. Wolverton, M. G. Kanatzidis, and L. D. Zhao, Ultrahigh power factor and thermoelectric performance in hole-doped single-crystal SnSe, *Science* **351**, 141 (2016).
- [15] C.-C. Lin, R. Lydia, J. H. Yun, H. S. Lee, and J. S. Rhyee, Extremely low lattice thermal conductivity and point defect scattering of phonons in Ag-doped (SnSe)_{1-x}(SnS)_x compounds, *Chem. Mater.* **29**, 5344 (2017).
- [16] Q. Zhang, E. K. Chere, J. Sun, F. Cao, K. Dahal, S. Chen, G. Chen, and Z. Ren, Studies on thermoelectric properties of n-type polycrystalline SnSe_{1-x}S_x by Iodine doping, *Adv. Energy Mater.* **5**, 1500360 (2015).
- [17] S. Liu, N. Sun, M. Liu, S. Sucharitakul, and X. P. A. Gao, Nanostructured SnSe: Synthesis, doping, and thermoelectric properties, *J. Appl. Phys.* **123**, 115109 (2018).
- [18] H. Ju, M. Kim, D. Park, and J. Kim, A strategy for low thermal conductivity and enhanced thermoelectric performance in SnSe: Porous SnSe_{1-x}S_x nanosheets, *Chem. Mater.* **29**, 3228 (2017).
- [19] M. R. Burton, T. Liu, J. McGettrick, S. Mehraban, J. Baker, A. Pockett, T. Watson, O. Fenwick, and M. J. Carnie, Thin film Tin Selenide (SnSe) thermoelectric generators exhibiting ultralow thermal conductivity, *Adv. Mater.* **30**, 1801357 (2018).
- [20] A.-T. Pham, T. H. Vu, C. Cheng, T. L. Trinh, J.-E. Lee, H. Ryu, C. Hwang, S.-K. Mo, J. Kim, L.-d. Zhao, A.-T. Duong, and S. Cho, High-quality SnSe₂ single crystals: Electronic and thermoelectric properties, *ACS Appl. Energy Mater.* **3**, 10787 (2020).
- [21] S. Saha, A. Banik, and Dr. K. Biswas, Few-layer nanosheets of n-type SnSe₂, *Chem. Eur. J.* **22**, 15634 (2016).
- [22] Y. Luo, Y. Zheng, Z. Luo, S. Hao, C. Du, Q. Liang, Z. Li, K. A. Khor, K. Hippalgaonkar, J. Xu, Q. Yan, C. Wolverton, and G. M., Kanatzidis, n-type SnSe₂ oriented-nanoplate-based pellets for high thermoelectric performance, *Adv. Energy Mater.* **8**, 1702167 (2018).
- [23] C. Zhou, Y. Yu, X. Zhang, Y. Cheng, J. Xu, Y. K. Lee, B. Yoo, O. Cojocar-Mirédin, G. Liu, S.-P. Cho, M. Wuttig, T. Hyeon, and I. Chung, Cu intercalation and Br doping to thermoelectric SnSe₂ lead to ultrahigh electron mobility and temperature-independent power factor, *Adv. Funct. Mater.* **30**, 1908405 (2019).
- [24] J. Chen, D. M. Hamann, D. Choi, N. Poudel, L. Shen, L. Shi, D. C. Johnson, and S. Cronin, Enhanced cross-plane thermoelectric transport of rotationally disordered SnSe₂ via Se-vapor annealing, *Nano Lett.* **18**, 6876 (2018).
- [25] T. J. Slade, J. A. Grovogui, J. J. Kuo, S. Anand, T. P. Bailey, M. Wood, C. Uher, G. J. Snyder, V. P. Dravid, and M. G. Kanatzidis, Understanding the thermally activated charge transport in NaPb_mSbQ_{m+2} (Q = S, Se, Te) thermoelectrics: Weak dielectric screening leads to grain boundary dominated charge carrier scattering, *Energy Environ. Sci.* **13**, 1509 (2020).
- [26] R. C. Neville, B. Hoeneisen, and C. A. Mead, Permittivity of strontium titanate, *J. Appl. Phys.* **43**, 2124 (1972).
- [27] D. I. Bilc, R. Orlando, R. Shaltaf, G.-M. Rignanese, J. Iniguez, and Ph. Ghosez, Hybrid exchange-correlation functional for accurate prediction of the electronic and structural properties of ferroelectric oxides, *Phys. Rev. B* **77**, 165107 (2008).
- [28] M. Goffinet, P. Hermet, D. I. Bilc, and Ph. Ghosez, Hybrid functional study of prototypical multiferroic bismuth ferrite, *Phys. Rev. B* **79**, 014403 (2009).
- [29] A. Prikockyte, D. Bilc, P. Hermet, C. Dubourdieu, and Ph. Ghosez, First-principles calculations of the structural and dynamical properties of ferroelectric YMnO₃, *Phys. Rev. B* **84**, 214301 (2011).

- [30] R. Dovesi, A. Erba, R. Orlando, C. M. Zicovich-Wilson, B. Civalleri, L. Maschio, M. Rerat, S. Casassa, J. Baima, S. Salustro *et al.*, Quantum-mechanical condensed matter simulations with CRYSTAL, *WIREs Comput. Mol. Sci.* **8**, e1360 (2018).
- [31] D. V. Oliveira, M. F. Peintinger, J. Laun, and T. Bredow, BSSE-correction scheme for consistent Gaussian basis sets of double- and triple-zeta valence with polarization quality for solid-state calculations, *J. Comput. Chem.* **40**, 2364 (2019).
- [32] J. Laun, D. V. Oliveira, and T. Bredow, Consistent Gaussian basis sets of double- and triple-zeta valence with polarization quality of the fifth period for solid-state calculations, *J. Comput. Chem.* **39**, 1285 (2018).
- [33] G. K. H. Madsen and D. J. Singh, BoltzTraP. A code for calculating band-structure dependent quantities, *Comput. Phys. Commun.* **175**, 67 (2006).
- [34] S. D. Kang and G. J. Snyder, Charge-transport model for conducting polymers, *Nat. Mater.* **16**, 252 (2017).
- [35] Y. Kajikawa, Analysis of high-temperature thermoelectric properties of p-type CoSb₃ within a two-valence-band and two-conduction-band model, *J. Appl. Phys.* **115**, 203716 (2014).
- [36] D. I. Bilc, S. D. Mahanti, and M. G. Kanatzidis, Electronic transport properties of PbTe and AgPb_mSbTe_{2+m} systems, *Phys. Rev. B* **74**, 125202 (2006).
- [37] I. G. Austin and N. F. Mott, Polarons in crystalline and non crystalline materials, *Adv. Phys.* **18**, 41 (1969).
- [38] H. J. Goldsmid and J. W. Sharp, Estimation of the thermal band gap of a semiconductor from Seebeck measurements, *J. Electron. Mater.* **28**, 869 (1999).
- [39] Y. Mao, X. Ma, D. Wu, C. Lin, H. Shan, X. Wu, J. Zhao, A. Zhao, and B. Wang, Interfacial polarons in van der Waals heterojunction of monolayer SnSe₂ on SrTiO₃ (001), *Nano Lett.* **20**, 8067 (2020).
- [40] H. Moon, J. Bang, S. Hong, G. Kim, J. Wook Roh, J. Kim, and W. Lee, Strong thermopower enhancement and tunable power factor via semimetal to semiconductor transition in a transition-metal dichalcogenide, *ACS Nano* **13**, 13317 (2019).
- [41] W. Y. Kim, H. J. Kim, T. Hallam, N. McEvoy, R. Gatensby, H. C. Nerl, K. O'Neill, R. Siris, G.-T. Kim, and G. S. Duesberg, Field-dependent electrical and thermal transport in polycrystalline WSe₂, *Adv. Mater. Interfaces* **5**, 1701161 (2018).
- [42] <http://www.melodica.spin.cnr.it/>.